IOP Publishing

Journal of Geophysics and Engineering

J. Geophys. Eng. **12** (2015) 1015–1023

doi:10.1088/1742-2132/12/6/1015

Seismic signatures of carbonate caves affected by near-surface absorptions

Ying Rao[1,2] and Yanghua Wang[2]

[1] State Key Laboratory of Petroleum Resources & Prospecting, China University of Petroleum (Beijing), People's Republic of China

[2] Centre for Reservoir Geophysics, Department of Earth Science and Engineering, Imperial College London, UK

E-mail: raoying@cup.edu.cn and yanghua.wang@imperial.ac.uk

Received 19 September 2015, revised 19 October 2015
Accepted for publication 21 October 2015
Published 2 December 2015

Abstract

The near-surface absorption within a low-velocity zone generally has an exponential attenuation effect on seismic waves. But how does this absorption affect seismic signatures of karstic caves in deep carbonate reservoirs? Seismic simulation and analysis reveals that, although this near-surface absorption attenuates the wave energy of a continuous reflection, it does not alter the basic kinematic shape of bead-string reflections, a special seismic characteristic associated with carbonate caves in the Tarim Basin, China. Therefore, the bead-strings in seismic profiles can be utilized, with a great certainty, for interpreting the existence of caves within the deep carbonate reservoirs and for evaluating their pore spaces. Nevertheless, the difference between the central frequency and the peak frequency is increased along with the increment in the absorption. While the wave energy of bead-string reflections remains strong, due to the interference of seismic multiples generated by big impedance contrast between the infill materials of a cave and the surrounding carbonate rocks, the central frequency is shifted linearly with respect to the near-surface absorption. These two features can be exploited simultaneously, for a stable attenuation analysis of field seismic data.

Keywords: near-surface absorption, attenuation, caves, carbonate reservoirs, *Q*

(Some figures may appear in colour only in the online journal)

Introduction

Prediction of caves, vugs and fractures is a key technology in characterization of karstic carbonate reservoirs. Karstic reservoirs tend to be distributed evenly along regional unconformities, mostly 0–50 m below the unconformity and in some cases up to 200–300 m below the unconformity. This is because the porosity in carbonate units below the unconformity was enhanced by the associated paleokarst processes. They were near-surface processes and later burial compaction and diagenesis (Loucks 1999). Resultant caves, vugs and fractures have been acted generally as store space and the oil and gas migration path. However, the complexity of the tectonic history and geologic settings strongly complicated the development and distribution of karsts and karstic reservoirs. There were meteoric dissolution and hydrothermal karstifications that had relative weak relationships with unconformities.

In this paper, we envisage 'caves' in karstic carbonate units. For pores of less than approximately 5 mm in diameter, they are often classified as fabric selective pores (Choquette and Pray 1970) as well as inter-particle and separate vug porosity (Lucia 1983). For pores of large than 5 mm, they are classified as non-fabric selective pores. For the latter class, the term 'vug' is used to describe pores larger than about 5 mm but not large enough to be recognized by conventional logging, arbitrarily defining this diameter to be 5–500 mm; the term 'cave' or 'huge cave' describe a pore space with a diameter of more than 500 mm (Zhao *et al* 2014). Within carbonate units, caves could cause strong scattering and diffraction in the seismic response. They are low-velocity anomalous bodies, but a significant phenomenon is that they do not necessarily show strong attenuation effect in seismic data.

This study targets the Tarim Basin, western China, where the seismic signatures of carbonate reservoirs have a typical

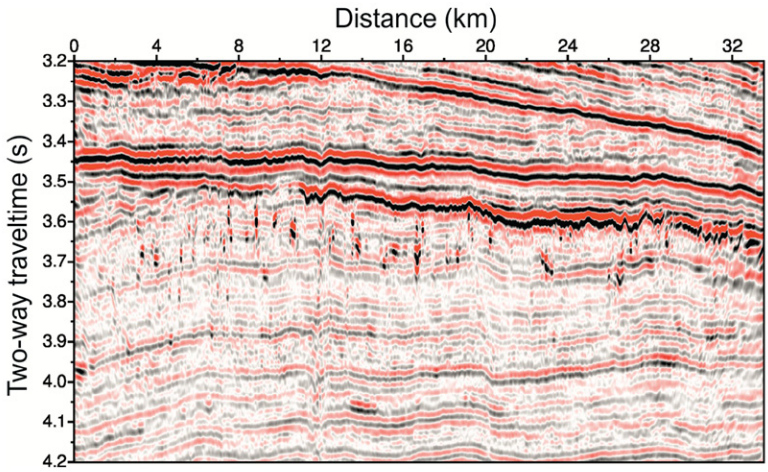

Figure 1. A seismic profile from the Tarim Basin, clearly showing the bead-string reflections, associated to karstic caves in the carbonate reservoir (between 3.55 and 3.75 s roughly), underneath a unconformity (at time 3.5 in the left and 3.65 s in the right).

characteristic of bead-string reflections (figure 1). This characteristic might be less shown in the other basins, but has been found in all carbonate reservoirs in the central, north and southwest parts of the Tarim Basin (Liu *et al* 2008, Yang *et al* 2012). The bead-strings that existed in reflection images have been used as a direct indicator for cave bodies with carbonate units.

In published literatures, most studies on bead-string reflections are only focused on the bead-string itself. However, the overlying structure and lithology in theory also affect the reliability and accuracy of reservoir characteristics. Particularly in the Tarim Basin, with enriched carbonate reservoirs, the modern time near-surface desert, consisted of loose sands, has a low velocity and a strong absorption. This near-surface absorption within low-velocity zone has an exponential attenuation effect on seismic waves. In logarithmic scale, the amount of attenuation per wavelength is (Wang 2008)

$$\frac{20\pi}{\ln(10)Q} \approx \frac{27.29}{Q} \quad (\text{dB}/\lambda), \tag{1}$$

where Q is the quality factor, and λ is the wavelength which is related to velocity. In expression 1, there are two key parameters: inverse-Q (or Q^{-1}), the absorption of the media and equivalently the attenuation of seismic waves, and wavelength λ which is related to the velocity. For example, given a near-surface velocity 2100 m s^{-1} and $Q = 20$, for the plane wave of frequency 40 Hz, the amplitude decreases by 3 dB as the wave travels 120 m, and the amplitude of a surface-recorded two-way reflection decreases in double by 6 dB at depth 120 m. In this paper, we investigate how this absorption within near-surface low-velocity zone affects the bead-string reflections of caves within deep carbonate reservoirs.

We use a frequency–domain wave equation method to simulate seismic wavefield from the area with different values of the near-surface absorption, which is presented as a complex velocity in the wave equation. We also perform reverse-time migration to reconstruct the seismic image of cave bodies. We demonstrate how the absorption within the near-surface media affects the shape, the energy, the central frequency of the bead-string reflections.

Wave equation including attenuation

The acoustic wave equation is defined in the frequency domain as (Wang and Rao 2006)

$$\left(\nabla^2 + \frac{\omega^2}{v^2(\mathbf{r})}\right)P(\mathbf{r}) = -S(\omega)\delta(\mathbf{r} - \mathbf{r}_s), \tag{2}$$

where $P(\mathbf{r})$ is the pressure wavefield at position $\mathbf{r}$, ∇^2 is the spatial Laplacian operator, $v(\mathbf{r})$ is the velocity, $S(\omega)$ is the source signature at position $\mathbf{r}_s$, and ω is the angular frequency. When considering the attenuation effect, the real-valued velocity is replaced with a complex velocity, and rewrite it as

$$\left(\nabla^2 + \frac{\omega^2}{c^2(\mathbf{r})}\right)P(\mathbf{r}) = -S(\omega)\delta(\mathbf{r} - \mathbf{r}_0), \tag{3}$$

where $c(\mathbf{r})$ is the complex velocity,

$$c(\mathbf{r}) = c_{\text{re}}(\mathbf{r}) + \text{i}c_{\text{im}}(\mathbf{r}). \tag{4}$$

The real part $c_{\text{re}}(\mathbf{r})$ is the ordinary velocity $v(\mathbf{r})$, as is used routinely in seismic analysis, and the imaginary part c_{im} carries the information we need for attenuation. Corresponding to the complex velocity, a complex-valued wavenumber is

$$k = \frac{\omega}{c_{\text{re}} + \text{i}c_{\text{im}}} = \frac{\omega c_{\text{re}}}{c_{\text{re}}^2 + c_{\text{im}}^2} - \text{i}\frac{\omega c_{\text{im}}}{c_{\text{re}}^2 + c_{\text{im}}^2}. \tag{5}$$

Then, the frequency component of a plane wave can be expressed as

$$\exp(\text{i}kx) = \exp\left(\text{i}\frac{\omega c_{\text{re}}x}{c_{\text{re}}^2 + c_{\text{im}}^2}\right)\exp\left(\frac{\omega c_{\text{im}}x}{c_{\text{re}}^2 + c_{\text{im}}^2}\right), \tag{6}$$

where x is the travel distance. The second exponential factor in the right-hand side represents the attenuation along the ray path, while the first term is related to the phase change. According to Aki and Richards (1980), the wave attenuation can be presented as

$$A(x) = A_0 \exp\left(-\frac{\omega x}{2c_{\text{re}}Q}\right), \tag{7}$$

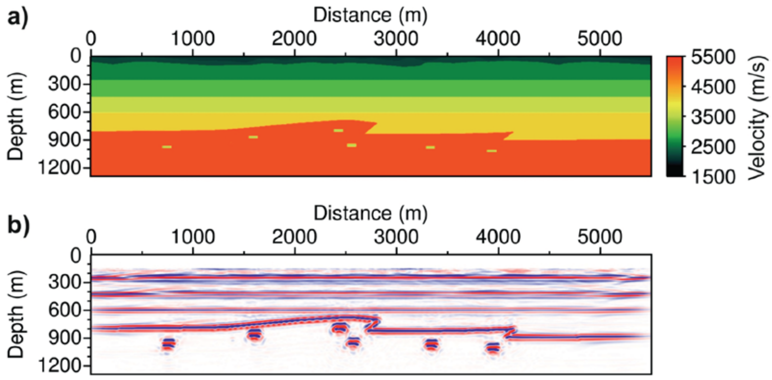

Figure 2. (a) A velocity model with six carbonate caves at 700–1000 m depth. (b) Seismic migration image of synthetic data without the absorption effect. There are strong bead-string reflections, corresponding to the six carbonate caves.

where A_0 is the initial amplitude of the plane wave at $x = 0$, and $A(x)$ is the amplitude at distance x. Direct comparison of the attenuation terms between expressions 6 and 7 leads to the following relationship between the attenuation (the inverse of Q) and the complex velocity:

$$Q^{-1} \approx -\frac{2c_{\mathrm{im}}}{c_{\mathrm{re}}}. \quad (8)$$

In this approximation, $c_{\mathrm{re}}^2 \gg c_{\mathrm{im}}^2$ is assumed (Rao and Wang 2009).

Wave equation (3) is solved using a finite difference method for individual frequencies in parallel. We use a rotated second-order finite-differencing operator which, together with the ordinary second order operator, produces a numerical result equivalent to a fourth order approximation (Štekl and Pratt 1998, Wang 2011). Once we obtain all frequency components of the wavefield at any spatial position, performing inverse Fourier transform with respect to the frequency variable will produce the time-domain seismic trace at this location. For a frequency-independent or so-called constant-Q model (Wang and Guo 2004), we simply replace a real velocity model in the wave equation. Therefore, the ordinary 2D finite-differencing scheme for the original frequency-domain wave equation is kept unchanged. The additional implication is just the manipulation and calculation of complex-valued matrices, related to complex velocity values. However, in order to model caves with difference thickness, a refined finite-difference scheme or alternative algorithms may be needed.

Bead-string reflections

A bead-string is basically a series of seismic multiple reflections generated by big impedance contrast between the infill materials of a cave and the surrounding carbonate rocks. Because this seismic signature is a stack of internal multiples within a cave, the near-surface attenuation will affect it differently than affect the seismic response of a continuous horizon reflector. When conditions (including the duration of the source wavelet, propagation angle, the size of caves, the impedance contrast etc) are properly met, the interference of these internal multiples will enhance the resultant amplitude. The enhancement is also unrelated to the near-surface attenuation, which is the same for either the cave multiples or a horizontal reflection at the same depth. Note that the amplitude of the horizontal reflection is also affected by focusing and defocusing effect of interfaces on the top of the current reflector (Wang and Houseman 1994).

We build a velocity model of 5500 m × 1300 m in size with 5.5 m grid size (figure 2(a)) to simulate seismic waves propagated through carbonate reservoirs in Tarim Basin. In the model, there are 7 layers in total, and the stratified velocities vary from 2100 to 5200 m s^{-1}. The velocities from the top to the bottom are 2100 m s^{-1}, 2200 m s^{-1}, 2600 m s^{-1}, 3000 m s^{-1}, 3600 m s^{-1}, 4100 m s^{-1} and 5200 m s^{-1}, respectively. These velocities correspond to weathered sand, water saturated sand, quaternary sandstone, mudstone, high porosity sandstone, tight sandstone and limestone, respectively.

Within the bottom layer, there are six cave bodies. The cave bodies could contain calcium carbonate mineral, and the velocity within cave bodies is set to be 3500 m s^{-1}. These caves are surrounded by the Ordovician carbonate rocks with a high velocity of 5200 m s^{-1}. Therefore, cave bodies have a large velocity contrast to the surrounding media. The height and width of the cave bodies are 16.5 m and 49.5 m, respectively. On top of the six cave bodies, there is a set of overthrusts.

To generate synthetic seismic data, 333 sources and 1000 receivers, with 16.5 m and 5.5 m intervals, respectively, are set along the top of the model. The source waveform is a Ricker wavelet with the peak frequency of 40 Hz. The time sampling is 0.5 ms.

In order to see the bead-string reflections, reverse-time migration (RTM) is performed on synthetic data. The resultant image (figure 2(b)) clearly shows the bead-string reflections which unambiguously indicate the cave positions. But in this first synthetic example, the absorption/attenuation effect is not considered yet.

The second example is a group of synthetics, corresponding to the same velocity model as figure 2(a) but with various near-surface absorptions. For the four shot gathers displayed in figure 3, the constant absorption/attenuation values within the near surface zone (between 0 and 250 m in depth) are set to be $Q^{-1} = 0.02$, 0.05, 0.1, 0.15, respectively.

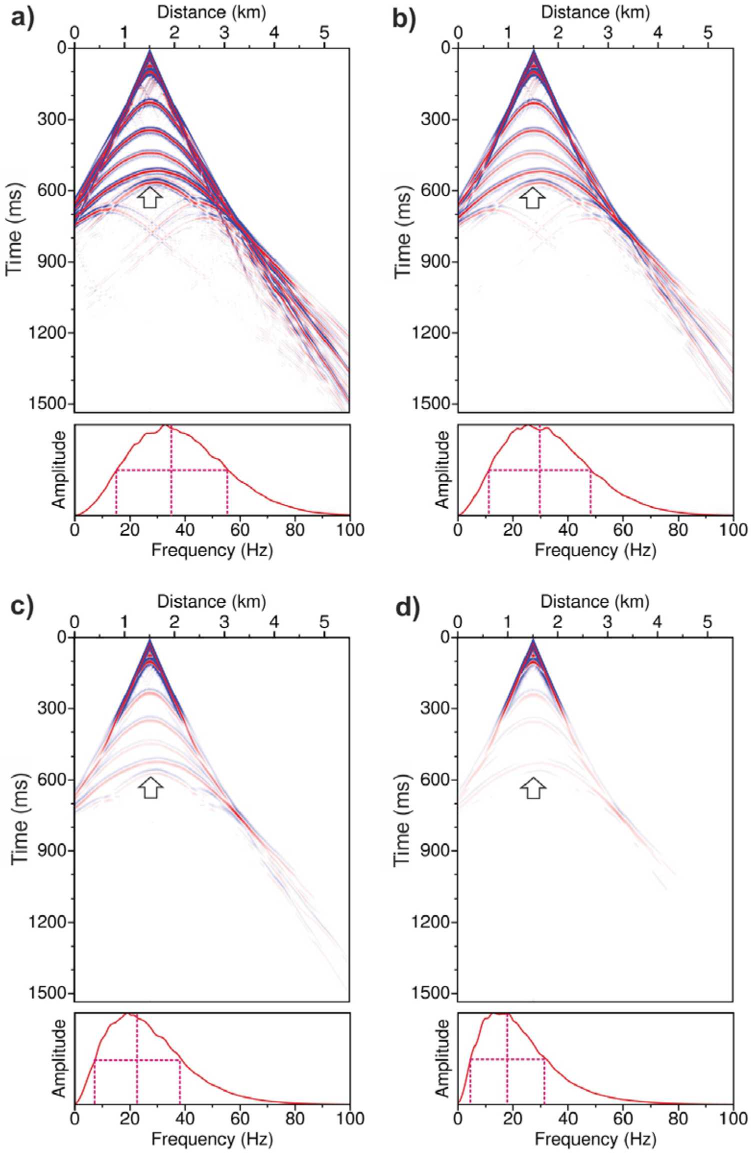

Figure 3. Synthetic shot-gathers and corresponding amplitude spectra. The synthetic data are generated from the velocity model figure 2(a), and the source is located at 1.5 km distance at the surface. The near-surface absorption Q^{-1} values between 0 and 250 m depth are (a) 0.02, (b) 0.05, (c) 0.1, and (d) 0.15, respectively. The dotted vertical lines in spectra indicate the frequency bands and the central frequencies, which obviously differ from the peak frequencies.

These Q^{-1} values cover possible variations of the near-surface lithology in the Tarim Basin. Intuitively, the amplitudes of a 40 Hz plane wave, reflected from 250 m depth, are decreased by $(2 \times 250/52.5) \times 27.3\,Q^{-1} \approx 5.2,\ 13,\ 26,\ 39$ dB, correspondingly. As we focus on the attenuation effect of near-surface absorptions, Q^{-1} is all set to be zero for the rest of depth below 250 m.

In order to see the near-surface Q effect to the seismic reflections, we simply mute out the first arrivals from the shot gathers, and analyze the frequency spectra. The amplitude spectra clearly demonstrate that the central frequency is gradually decreased, when the absorption/attenuation Q^{-1} within the near-surface zone is increased from 0.02 to 0.15.

Wang (2015a) proved that the central frequency is very close to the mean frequency. Therefore, the central frequency is approximated by the mean frequency, statistically estimated from the discrete power spectrum:

$$f_c \approx \frac{\int_0^\infty f A^2(f)\mathrm{d}f}{\int_0^\infty A^2(f)\mathrm{d}f}, \tag{9}$$

where $A^2(f)$ is the power spectrum. The central frequency of a Ricker wavelet with 40 Hz peak frequency is 42.4 Hz. Due to the attenuation effect caused by the near-surface absorption, the central frequency is shifted to 35.5, 29.2, 21.9, 17.1 Hz, respectively, in the four synthetic shot gathers.

As shown obviously in figure 3, the central frequency, the geometric center of the frequency band (the vertical dashed lines), differ from the peak frequency. For a Ricker wavelet,

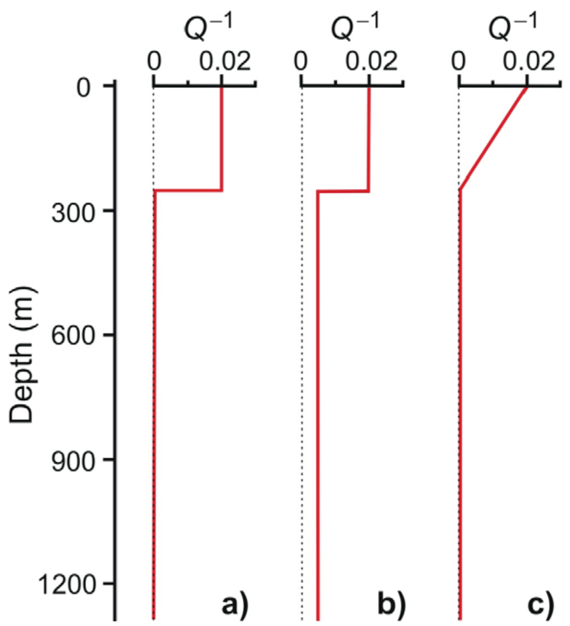

Figure 4. Three schematic models of Q^{-1} variable along the depth. (a) In the first group of tests, for the near-surface depth above 250 m, Q^{-1} is equal to 0.02, 0.05, and 0.1, respectively, and for depth below 250 m, Q^{-1} is equal to zero. (b) In the second group of tests, for the near-surface depth above 250 m, Q^{-1} is equal to 0.02, 0.05, and 0.1, respectively, and for the depth below 250 m, Q^{-1} is equal to 0.005. (c) In the third group of tests, for the near-surface depth above 250 m, Q^{-1} is linearly decreased from 0.02, 0.05, and 0.1 to zero, respectively, and for the depth below 250 m, Q^{-1} is equal to zero.

according to Wang (2015b), the relationship between a central frequency and a peak frequency is

$$f_c \approx 1.059\, f_p. \tag{10}$$

where f_c and f_p are the central frequency and the peak frequency. However, figure 3 shows that the difference between the central frequency and the peak frequency is increased. It clearly indicates that wavelets, affected by the near-surface absorption, are no longer a standard Ricker wavelet set at the source point. There are two implications. First, relationship (10) that is valid for a Ricker wavelet is not satisfied any more. Second, the frequency shifting technique for Q estimation, if it is based on a Ricker wavelet assumption, will not work in practice for field seismic data. Wang (2015c) generalized those wavelets systematically using fractional derivatives of a Gaussian function, and defines the peak frequency as

$$f_p = f_0\sqrt{\frac{u}{2}}, \tag{11}$$

where u is the order of a time-domain derivative, and f_0 is a reference frequency (in radians per second). When u is an integer 2, it is the Ricker wavelet, for which equation (11) becomes $f_p = f_0$. When u decreases, the difference between f_p and f_0 is increased.

The arrows point at the diffraction of a cave directly underneath a surface source at 1.5 km distance. In these shot gathers, it is difficult to see any expected string of beads. Since the expected string of beads cannot be seen clearly from any shot gathers, in the following sections, we examine the attenuation effect in migration profiles.

The attenuation effects on seismic signatures

To investigate the effect of near-surface absorptions, affecting bead-string reflections related to deep cave bodies, three test groups are designed. Figure 4 shows the absorption models schematically, in which Q^{-1} varies along with the depth, corresponding to three different test groups:

(1) In test group 1, the absorptions (Q^{-1}) within near-surface zone (0–250 m depth) are equal to 0.02, 0.05 and 0.1, respectively. The absorption below the depth of 250 m is equal to zero.
(2) In test group 2, the near-surface absorptions are equal to 0.02, 0.05 and 0.1, respectively. They are the same as that in the first group. However, the absorption in the rest depth (below 250 m) is set to be 0.005.
(3) In test group 3, the absorptions within the top 250 m depth are linearly decreased, from either 0.02, 0.05 or 0.1, down to zero. The absorption below the 250 m depth is zero.

The near-surface strong absorption model represents the near-surface desert, consisting of loose sands, in the Tarim Basin. The effects of near-surface absorptions will appear in the shape change, phase delay, the energy decay and the central frequency shift of bead-string reflections of deep caves.

The shape of bead-string reflections

Figures 5–7 are seismic profiles after reverse-time migration (RTM), using forward modelling seismic data based on the three test groups of absorption models above. The RTM algorithm is based on the 2D acoustic wave equation, and is implemented using a finite-difference method. The RTM algorithm does not include the absorption coefficients, and the data have not been pre-processed with inverse Q filtering, before being fed into the RTM for migration.

After migration, all diffraction of caves are focused (figures 5–7), and thus the imaged caves seem stronger than the shallow reflections. In contrast, the shallow reflections are stronger than the cave reflections/diffractions in shot gathers (figure 3). Note that figures 5–7 are displayed in the same amplitude scale.

These seismic profiles show the seismic reflection characteristics of carbonate reservoirs:

(1) Within each figure, from the top to the bottom, when the absorption value Q^{-1} in the near-surface zone (0–250 m) is increased, the amplitude of bead-string reflections of caves is decreased.
(2) The bead-string reflections in test group 2 (figure 6) are slightly weaker than test group 1 (figure 5). This is because the absorption Q^{-1} in the depth blow 250 m is non-zero valued.
(3) The bead-string reflections in test group 3 (figure 7) are stronger than either test group 1 (figure 5) or test group 2

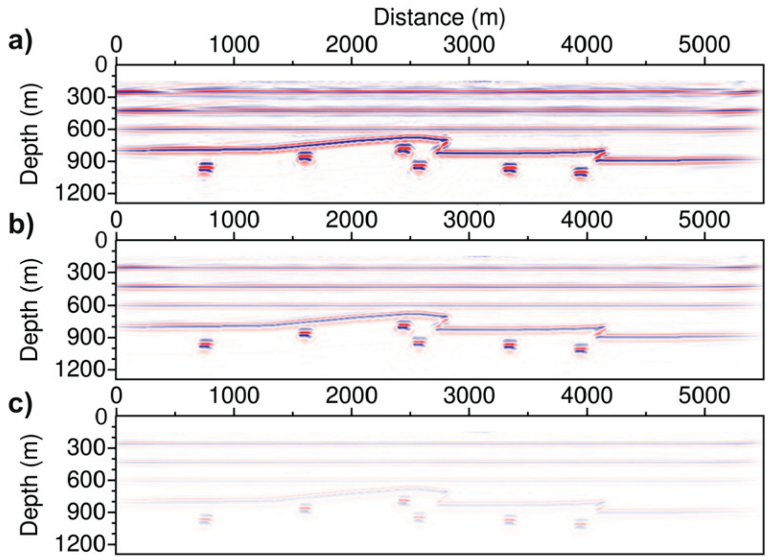

Figure 5. Seismic images of test group 1: for the depth above 250 m, Q^{-1} is equal to (a) 0.02, (b) 0.05, (c) 0.1, respectively, and for depth below 250 m, Q^{-1} is equal to zero. The reflection energy is generally decreased as Q^{-1} increasing. Strong bead-string reflections correspond to carbonate caves.

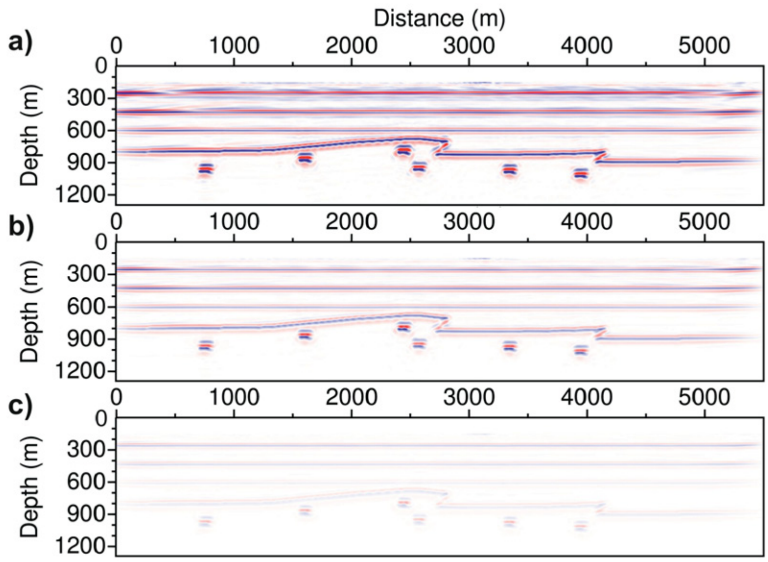

Figure 6. Seismic image of test group 2: for the depth above 250 m, Q^{-1} is equal to (a) 0.02, (b) 0.05, (c) 0.1, respectively, for depth between 250 and 600 m, Q^{-1} is equal to 0.005, and for the rest, Q^{-1} is equal to zero. The bead-string reflections, corresponding to the carbonate caves, are weaker than the counterpart in figure 5, because of non-zero Q^{-1} in the middle part between 250 and 600 m.

(figure 6). This is because the integrated absorption in the shallow zone (0–250 m) is the smallest in the test group 3, in comparison the rest two groups.

Having said that the amplitudes of bead-string reflections, corresponding to deep caves, depend upon the accumulated absorption started from the top most, the waveforms of these bead-string reflections have similar phase and shape in all three test groups. This observation suggests very positively that, in practice, the near-surface absorption media will not affect the existence and the geometry of bead-string reflections of deep caves within carbonate media. However, this observation is not conclusive, unless there are strong lateral absorption changes in the overburden.

The phase delay

Figure 8 compares seismic responses of caves, corresponding to the three test groups above. For each group, from the top to the bottom, four panels are seismic responses of caves at the horizontal distance 707 m, 3298 m, 3903 m, 2533 m, respectively. Within each panel, there are seismic responses of caves corresponding to, from the left to the right, $Q^{-1} = \{0.15, 0.1, 0.05, 0.02, 0.0\}$ within the near-surface zone (0–250 m).

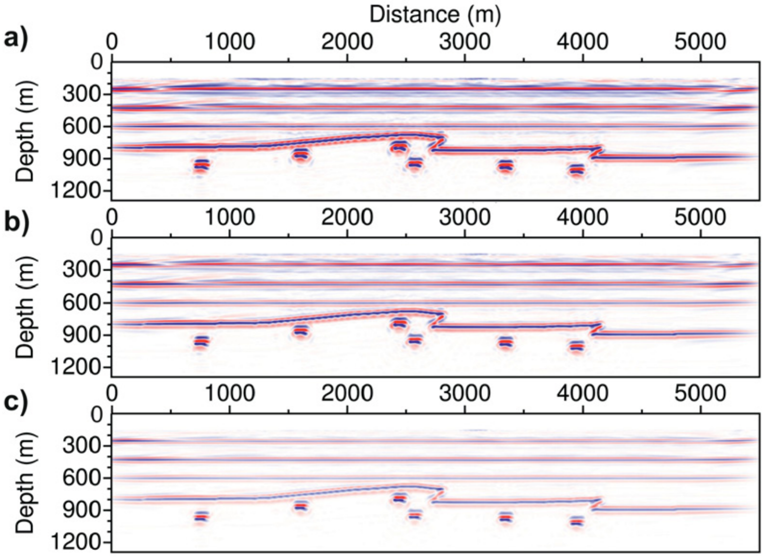

Figure 7. Seismic image of test group: for the depth above 250 m, Q^{-1} is linearly decreased from (a) 0.02, (b) 0.05, (c) 0.1, respectively, down to zero, for the depth below 250 m, Q^{-1} is equal to zero. The bead-string reflections, corresponding to the carbonate caves, are stronger than the counterparts in both tests 1 and 2. That is because the integral of attenuation Q^{-1} in the near-surface part is less than any of the previous two tests.

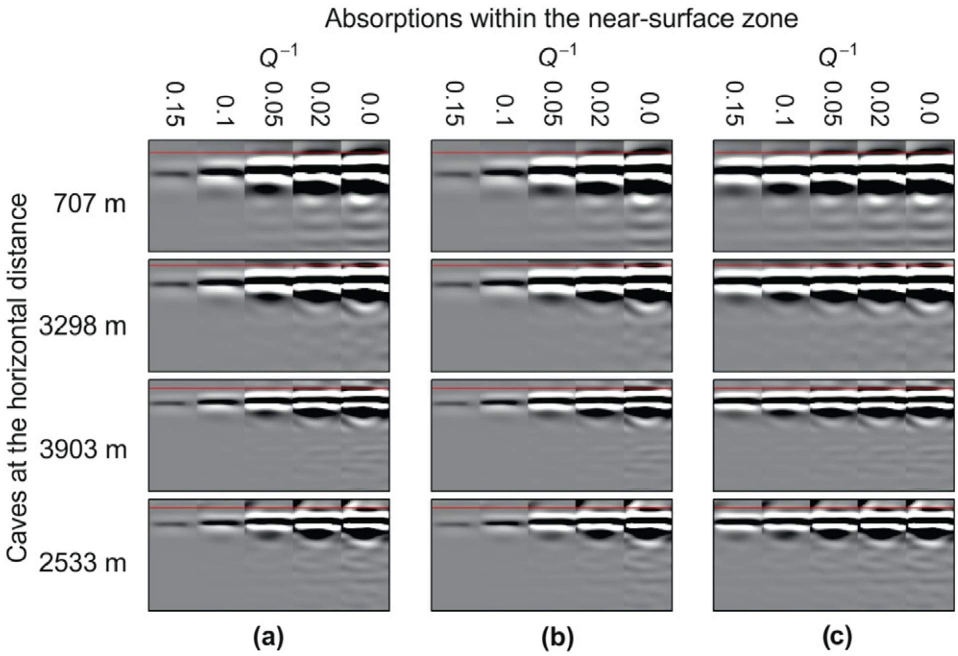

Figure 8. Comparison of seismic response of fracture-caves. (a)–(c) correspond to the three test groups 1, 2, 3. For each group, from the top to the bottom, four panels are seismic responses of caves at the horizontal distance 707, 3298, 3903, 2533 m, respectively. Within each panel, seismic responses (from the left to the right) correspond to $Q^{-1} = \{0.15, 0.1, 0.05, 0.02, 0.0\}$ within the near-surface zone (0–250 m). Near-surface absorptions cause time delay in the bead-string reflections of deep caves.

Because of associated velocity dispersion effect, near-surface absorptions cause time delay in the bead-string reflections of deep caves. According to the definition of Q^{-1} (equation (8)), the phase term in equation (6) becomes

$$\exp\left(\mathrm{i}\frac{\omega c_{\mathrm{re}} x}{c_{\mathrm{re}}^2 + c_{\mathrm{im}}^2}\right) \approx \exp\left(\mathrm{i}\frac{\omega t}{1 + \frac{1}{4}Q^{-2}}\right), \tag{12}$$

where $t = x/c_{\mathrm{re}}$. Non-zero Q^{-1} will delay the phase by a factor of $\left(1 + \frac{1}{4}Q^{-2}\right)^{-1}$. High value of Q^{-1} causes more time delay (the difference between the peak of the waveform and the reference time line in red). Particularly, when $Q^{-1} = 0.15$ and 0.1, bead-string reflections of caves at all four positions show clearly time-delay from no-attenuation case $Q^{-1} = 0.0$.

Within each test (a, b or c), the bead-string reflections of the four caves show detailed difference in the amplitude patterns among them. However, we hardly see the shape difference of these bead-string reflections of deep caves among three tests, especially if applying AGC (auto-gain controlling) to the data.

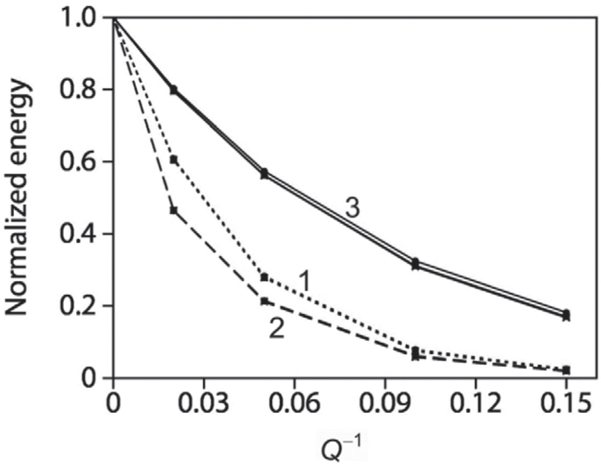

Figure 9. Normalized energy of bead-string reflections versus the near-surface absorption. The dotted curves, the dashed curves and the solid curves correspond to three test groups 1, 2 and 3, respectively. Within each group, the curves of four caves are similar and thus are overlaid each other.

The energy decay

Figure 9 displays normalized energy of bead-string reflections versus the near-surface absorption Q^{-1}. The dotted, dashed and solid curves correspond to three test groups 1, 2 and 3, respectively. The energy decay is generally close to an exponential function with Q^{-1}. This is consistent with the expectation described by equation (1). Although different values of the near-surface absorption are used, the attenuation curves within each group are similar and are overlaid each other.

Direct comparison among three test groups shows that the energy decay rate depends upon the total absorption accumulated within the overburden. For example, the energy curves of test group 3 are decayed most slowly, in contrast to other twos. This is one of fundamental mechanisms for seismic Q analysis, in which the slope of the logarithmic energy decay is treated as the attenuation Q^{-1} (Wang 2004).

The central frequency shifting

Note that seismic images obtained using reverse-time-migration (RTM) are presented in the depth axis. Thus the Fourier spectrum of a seismic trace is not in the temporal frequency domain, but in the spatial-frequency domain (i.e. the wavenumber domain, the Fourier transform with respect to the depth). In order to make comparison, the spatial frequency of a RTM trace is normalized to 42.36 Hz, which is the central frequency of the source Ricker wavelet, defined by 40 Hz peak frequency.

Figure 10 depicts the central frequency of bead-string reflections versus the near-surface absorption. Although different forms of the absorption variation are used, the central frequency of bead-string reflections of deep caves is decreased almost linearly, when the near-surface absorption Q^{-1} is increased.

Figure 10 also shows that the decrement rate of the central frequency of bead-string reflections, with respect to Q^{-1}, is increased, when the accumulated Q^{-1} value within

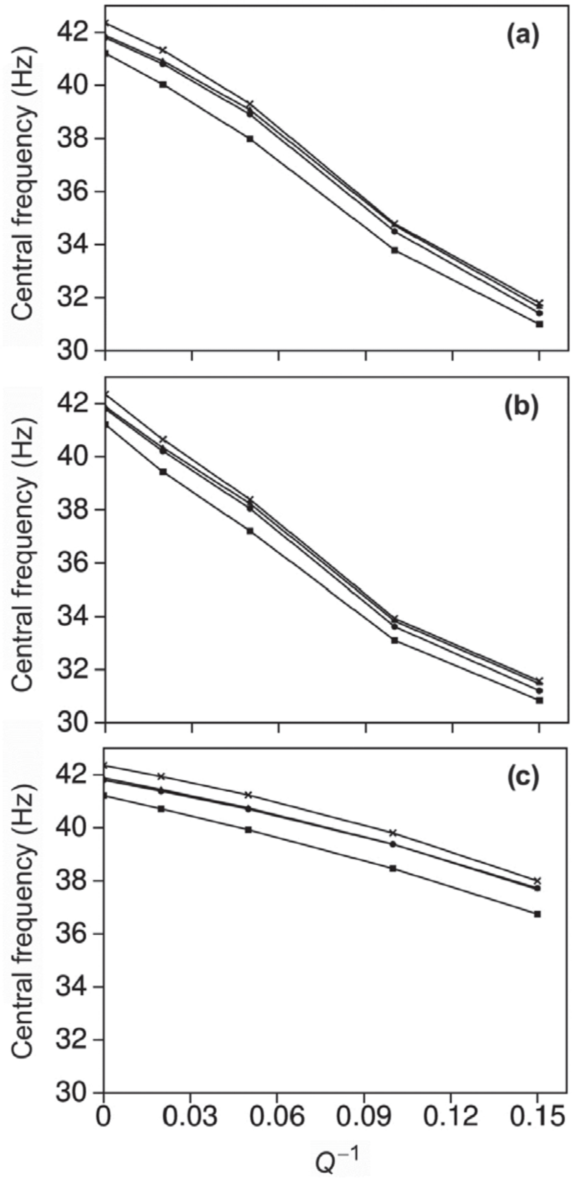

Figure 10. Comparison of the central frequencies of bead-string reflections of the deep caves. (a)–(c) correspond to test groups 1, 2, and 3, respectively. The cross, circle, triangle, rectangle marks correspond to 4 caves (at the horizontal distance 707, 3298, 3903, 2533 m) in the model. In general, the central frequency is decreasing as the accumulated Q^{-1} above is increased.

the overburden is increased. The test group 2 has the biggest cumulative value of Q^{-1} in the overburden, if compared to groups 1 and 3.

It is worthwhile to notice that the decrement rate of the central frequency, with respect to Q^{-1}, in migrated images (figure 10) is different from that in shot gathers (figure 3). This is because a migration image is ideally the reflectivity profile of subsurface interfaces, as the RTM imaging is made as the ratio of the reflection wavefield to the incident wavefield. The investigation in this paper indicates that Q estimations from RTM images are different from raw shot gathers. Any Q model estimated from migrated seismic data should be treated as a processing parameter, used in the resolution enhancement by inverse Q filtering.

Conclusions

This paper has simulated seismic wave propagation through caves in a deep carbonate reservoir. The prime objective is to evaluate how the absorption within the near-surface low-velocity zone affects seismic signatures of caves in deep reservoirs. A rather positive observation is that the near-surface absorption Q^{-1} does not alter the kinematic shape of bead-string reflections. This means that characteristics of bead-string reflections can be utilized with a great certainty, to judge the existence of deep caves and to evaluate the store space within carbonate units.

In general, the difference between the central frequency and the peak frequency is increased along with the increment of Q^{-1}. While the wave energy of bead-string reflections of a cave remains strong, due to the interference of multiples within the cave, the central frequency has a linear shifting trend, as the near-surface absorption Q^{-1} is increased. These two features can be exploited simultaneously, for achieving a stable Q estimation from field seismic data. However, even the source is a Ricker wavelet, seismic wavelet affected by the near-surface absorption is no longer a standard Ricker wavelet, and a frequency shifting technique for Q estimation will not work in practice, if it is based on a Ricker wavelet assumption. However, the change in wavelet shape might not significantly affect the shape of bead-string reflections, as they are fundamentally stacks of multiple reflections.

Further studies on the near-surface absorption effect will be to investigate seismic responses of caves with different infill materials, different elastic properties (both inside the cave and outside the cave, and different heterogeneity in the overburden, and to investigate seismic responses of vugs and fractures, which have smaller scale than caves, in carbonate reservoirs. Studies should be also on the imaging technology for caves in an environment with a complex overburden, smaller impedance variations (or some sort of transition zone) between cave and surrounding material.

Acknowledgments

That authors are grateful to the National Natural Science Foundation of China (grant no. 41474111), Science Foundation of China University of Petroleum Beijing (no. 2462015YQ0504), and the sponsors of the Centre for Reservoir Geophysics, Imperial College London, for supporting this research.

References

Aki K and Richards P G 1980 *Quantitative Seismology: Theory and Methods* (San Francisco, CA: WH Freeman)
Choquette P W and Pray L C 1970 Geologic nomenclature and classification of porosity in sedimentary carbonates *AAPG Bull.* **54** 207–50
Liu X P, Yang X L, Zhang Y Z and Han L 2008 Application of spectral decomposition to detection of fracture-cavity carbonate reservoir beds in the Tahe Oilfield, Tarim Basin, NW China *Acta Geol. Sin.* **82** 530–6
Loucks R G 1999 Paleocave carbonate reservoirs: origins, burial-depth modifications, spatial complexity, and reservoir implications *AAPG Bull.* **83** 1795–834
Lucia F J 1983 Petrophysical parameters estimated from visual descriptions of carbonate rocks: a field classification of carbonate pore space *J. Pet. Technol.* **35** 629–37
Rao Y and Wang Y 2009 Fracture effects in seismic attenuation images reconstructed by waveform tomography *Geophysics* **74** R25–34
Štekl I and Pratt R G 1998 Accurate viscoelastic modeling by frequency domain finite-difference using rotated operators *Geophysics* **63** 1779–94
Wang Y 2004 *Q* analysis on reflection seismic data *Geophys. Res. Lett.* **31** L17606
Wang Y 2008 *Seismic Inverse Q filtering* (Oxford: Blackwell)
Wang Y 2011 Seismic waveform modelling and tomography *Encyclopaedia of Solid Earth Geophysics* ed H Gupta (Berlin: Springer) pp 1290–301
Wang Y 2015a Frequencies of the Ricker wavelet *Geophysics* **80** A31–7
Wang Y 2015b The Ricker wavelet and the Lambert *W* function *Geophys. J. Int.* **200** 111–5
Wang Y 2015c Generalized seismic wavelets *Geophys. J. Int.* **203** 1172–8
Wang Y and Guo J 2004 Modified Kolsky model for seismic attenuation and dispersion *J. Geophys. Eng.* **1** 187–96
Wang Y and Houseman G A 1994 Inversion of reflection seismic amplitude data for interface geometry *Geophys. J. Int.* **117** 92–110
Wang Y and Rao Y 2006 Crosshole seismic waveform tomography: I. Strategy for real data application *Geophys. J. Int.* **166** 1224–36
Yang P, Sun Z D, Liu Y L, Li H Y, Dan G G and Jia H Q 2012 Origin and architecture of fractured-cavernous carbonate reservoirs and their influences on seismic amplitudes *Leading Edge* **31** 140–50
Zhao W Z, Shen A J, Qiao Z F, Zheng J F and Wang X F 2014 Carbonate karst reservoirs of the Tarim Basin, northwest China: types, features, origins, and implications for hydrocarbon exploration *Interpretation* **2** SF651–90